The Growth Kinetics of TiO$_2$ Nanoparticles from Titanium(IV) Alkoxide at High Water/Titanium Ratio

Gerko Oskam,[†] Abhinav Nellore, R. Lee Penn,[‡] and Peter C. Searson*

Department of Materials Science and Engineering, Johns Hopkins University, Baltimore, Maryland 21218
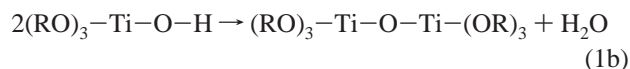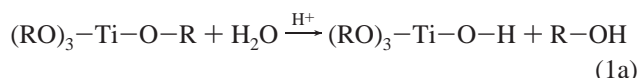
Received: May 16, 2002

We report on the growth kinetics of TiO$_2$ nanoparticles synthesized from aqueous solution using titanium-(IV) isopropoxide as precursor. The radius of primary particles was found to be between 1.5 and 8 nm, and the average particle radius cubed is shown to increase linearly with time in agreement with the Lifshitz-Slyozov-Wagner model for coarsening. The rate constant for coarsening increases with temperature due to the temperature dependence of the viscosity of the solution and the equilibrium solubility of TiO$_2$. At longer times and higher temperatures, secondary particles formed by epitaxial self-assembly of primary particles were observed with high-resolution transmission electron microscopy. The number of primary particles per secondary particle increases with time, and the percentage of primary particles present in the colloid decreases with increasing temperature.

Introduction

Metal oxide nanoparticles are important in a wide range of applications such as catalysis, cell separations, environmental remediation, and solar energy conversion. The electrical and optical properties of nanoparticles are often size dependent and, hence, it is essential to be able to control the particle size, shape, and size distribution.[1−8] This requires a detailed understanding of the mechanisms of nucleation and growth, as well as processes such as aggregation and coarsening. Solution phase synthesis from homogeneous solution[9−23] has been used to synthesize a variety of metal oxides including TiO$_2$,[12−23] ZnO,[25,26] iron oxides [e.g., ref 27], and oxyhydroxides [e.g., ref 28].

The formation of TiO$_2$ from titanium(IV) alkoxide proceeds via an acid-catalyzed hydrolysis step followed by condensation:[12−23]

$$(RO)_3{-}Ti{-}O{-}R + H_2O \xrightarrow{H^+} (RO)_3{-}Ti{-}O{-}H + R{-}OH$$
(1a)

$$2(RO)_3{-}Ti{-}O{-}H \rightarrow (RO)_3{-}Ti{-}O{-}Ti{-}(OR)_3 + H_2O$$
(1b)

The synthesis of titanium dioxide particles from titanium alkoxide precursors has been studied extensively.[17−23] In general, two regimes are distinguished: synthesis with a low water-to-titanium mole ratio, r, and synthesis with a high water-to-titanium mole ratio. For $r < 10$, spherical, relatively monodisperse aggregates of nanocrystallites with diameters of 0.5−1 m are obtained.[17−21] The growth kinetics of the aggregates are determined by the stability of the colloid [e.g., refs 17−19, 24].

At high r, hydrolysis of titanium alkoxide is very fast and nucleation and growth are completed within seconds.[17−21] The TiO$_2$ particles formed are unstable and a white suspension is immediately formed due to the precipitation of large aggregates. Peptization at elevated temperature in the presence of chloride or nitrate can be used to break up the aggregates into very small aggregates (<20 nm) and primary particles.[20,21] After this step, the TiO$_2$ primary particles are crystalline and consist mainly of anatase.[7,8,14,15,22,23] After peptizing, the colloidal dispersions are generally stable over periods of several weeks.

In solution phase synthesis, processes such as coarsening and aggregation can compete with nucleation and growth in modifying the particle size distribution in the system. Coarsening involves the growth of larger particles at the expense of smaller particles (also known as Ostwald ripening).[29−31] Epitaxial assembly results in the formation of large secondary particles from oriented primary particles.[28,32,33] In this paper, we report on the synthesis of TiO$_2$ nanoparticles. The time and temperature dependence of the primary particle size, size distribution, and assembly order are analyzed quantitatively.

Experimental Section

Anatase particles were prepared by precipitation from homogeneous solution using titanium(IV) isopropoxide as precursor in aqueous solution acidified with nitric acid to pH 1 using a water-to-titanium mole ratio of about 200.[14,15,20−23] Upon addition of titanium(IV) isopropoxide to the aqueous solution, a white suspension was immediately formed. Subsequently, the suspension was peptized at 85 °C in order to disperse the aggregates into primary particles and small aggregates (<20 nm).[20,21] During this step, evaporation of 2-propanol during hydrolysis (eq 1a) and some water results in condensation of the colloid. The resulting colloid was light blue, translucent, and was stable for several weeks. Particle growth was achieved by heating the resulting colloid to temperatures ranging from 160 °C to 220 °C for up to 300 h in a titanium pressure vessel. A typical procedure was as follows: 15 mL of Ti−(O−iPr)$_4$ was added dropwise to 185 mL of distilled, deionized water acidified with 1.3 mL of concentrated HNO$_3$ with vigorous

* Corresponding author. E-mail: searson@jhu.edu.
† Present address: Departamento de Física Aplicada, CINVESTAV-IPN Unidad Mérida, A. P. 73 Cordemex, Mérida, Yuc. 97310, Mexico. E-mail: oskam@mda.cinvestav.mx.
‡ Department of Earth and Planetary Sciences, JHU. Present address: Department of Chemistry, University of Minnesota, Minneapolis, MN 55455.

Growth Kinetics of TiO₂ Nanoparticles

J. Phys. Chem. B, Vol. 107, No. 8, 2003 **1735**

stirring at room temperature. The suspension was then peptized at 85 °C with stirring in an open Erlenmeyer flask for about 12 h until a final volume of 50 mL was reached. The colloid was then heated at an elevated temperature in a closed titanium pressure vessel for 4 to 300 h. Particle growth under these hydrothermal conditions resulted in a milky-white colloid with a TiO₂ concentration of about 80 g L^{-1}. The colloids were stable for several weeks.

The TiO₂ particles were characterized using a Philips CM300FEG transmission electron microscope (TEM). Samples were prepared in the following way. After particle growth at elevated temperatures, the resulting colloids were diluted by a factor 10^5 with 1 mM HNO₃ in water such that the final pH was about 3. One drop of the resulting colloid was placed on 400 mesh copper TEM grids coated with holey carbon and allowed to evaporate. TEM images were taken at a minimum of 5 different locations on the grid, and a total of 15−20 images were analyzed per sample. A minimum of 500 particles were measured per sample to ensure good statistics. The Philips CM300FEG TEM was equipped with a Gatan Imaging Filter (GIF) for energy-filtered imaging. All TEM images were collected using a Gatan CCD and Digital Micrograph software. Zero-loss TEM images in this work were formed using an energy-filtering technique that excludes electrons that have undergone significant energy losses due to inelastic scattering events (e.g., inner-shell ionization and plasmon interactions). The electron beam passes through a magnetic prism and is spread as a function of kinetic energy. By using an energy window of 10 eV centered about the accelerating voltage of the microscope, only low-loss (e.g., phonon scattering events) and zero-loss (elastic scattering events) are included in a zero-loss image. The exclusion of higher-loss electrons improves image resolution and contrast.[34]

X-ray diffraction (XRD) was performed on a Philips powder diffractometer (PW1729/PW1710/PW2773 generator/goniometer/detector). Samples were prepared by evaporating several drops of the colloid (80 g L^{-1} TiO₂) onto the unpolished backside of a silicon wafer. Scans were generally performed using an interval of 0.01° and an integration time of 3 s. The instrument broadening, determined using crystalline silicon powder (325 mesh, Alfa-Aesar), was about 0.06°.

Results and Discussion

Figure 1a shows a TEM image of as-prepared anatase particles. The average particle radius is 1.55 nm and the interference patterns illustrate that the particles are crystalline. Figure 1 also shows images of particles grown at 160 °C and 200 °C for 16 h illustrating that the particle size increases with growth temperature.

Figure 2 shows the average particle radius versus time at 160 °C and 200 °C. The particle radius increases with time from 1.55 nm for the as-prepared particles to 3.7 nm after 125 h at 200 °C. The vertical bars represent the standard deviation in the average particle size, which also increases with time. Figure 3 shows the particle size distributions for TiO₂ particles synthesized at 200 °C as a function of time. The histograms are approximately Gaussian in shape, and show that the particle size and the width of the size distribution increase with time. We note that the particle sizes obtained from TEM images (Figures 2 and 3) were restricted to primary particles and hence do not include secondary particles formed by epitaxial attachment (see below).

The Lifshitz-Slyozov-Wagner (LSW) model for coarsening provides a quantitative treatment of the time dependence of the
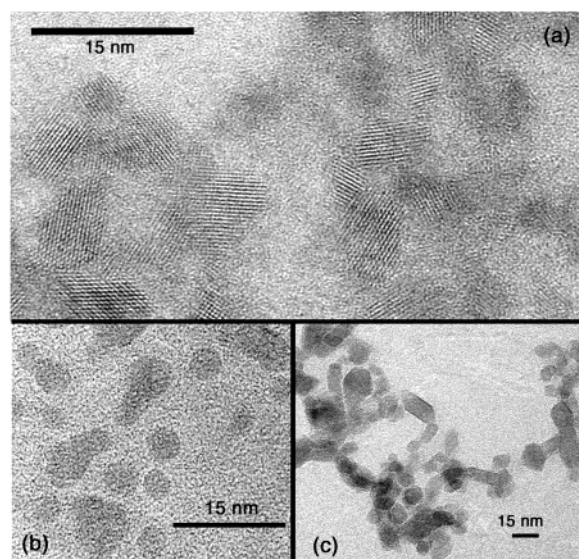

Figure 1. High-resolution TEM images of TiO₂ (anatase) particles: (a) as-prepared particles after peptizing at 85 °C for 14 h; (b) after growth at 160 °C for 16 h; (c) after growth at 200 °C for 16 h.
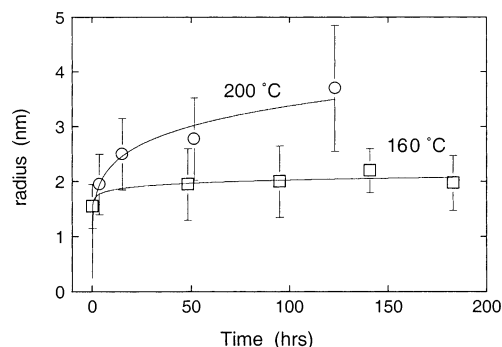

Figure 2. The average radius of primary particles as a function of growth time for 160 °C and 200 °C. The vertical bars indicate the standard deviation of the particle size distribution.

particle size and the size distribution.[30,31] Coarsening is driven by the dependence of the solubility of a solid phase on the particle size according to the Gibbs−Thomson relation. Assuming that the particles are spherical, the solubility, c_r, of a particle with radius r is given by

$$c_r = c_\infty \exp\left(\frac{2\gamma V_m}{RT}\frac{1}{r}\right) \qquad (2)$$

where c_∞ is the solubility at a flat surface, γ is the surface energy of the solid, V_m is the molar volume, R is the gas constant, and T is the temperature. For the case where $(2\gamma V_m/rRT) < 1$ such that the exponential term in eq 2 can be linearized, and assuming that the growth rate is determined by diffusion of the solute from the smaller particles to the larger particles, the following rate law is obtained:[30,31]

$$\bar{r}^3 - \bar{r}_0{}^3 = \frac{8\gamma D V_m{}^2 c_\infty}{9RT}t \qquad (3)$$

where $\bar{r}$ is the average particle radius at time t and $\bar{r}_0$ is the average particle radius at time zero.

Figure 4 shows the cube of the average particle radius obtained from TEM images (Figure 2) plotted versus time. The linear dependence shows that the increase in average particle size of anatase primary particles is dominated by diffusion-
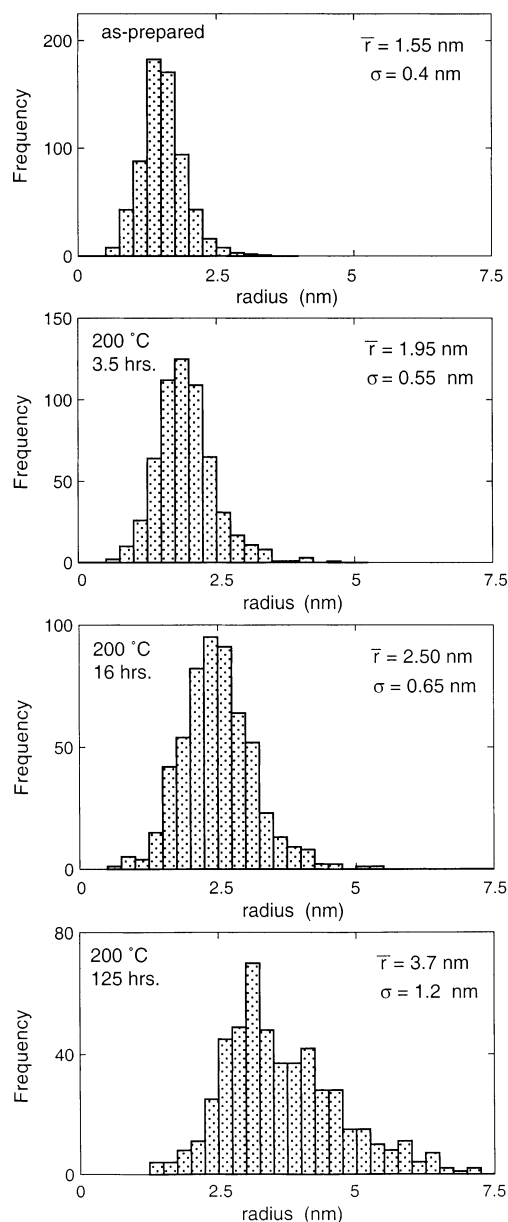
Figure 3. Primary particle size distributions for as-prepared and grown anatase particles as a function of aging time. The average radius, $\bar{r}$, and the standard deviation, σ, are indicated. TEM images were taken at a minimum of 5 different locations on the grid, and a total of 15–20 images were analyzed per sample. A minimum of 500 particles were measured per sample.
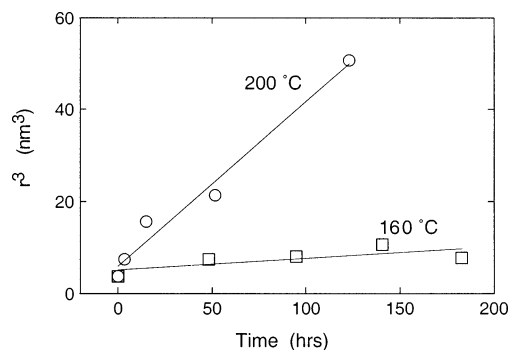

Figure 4. The results from Figure 2 re-plotted as the particle radius cubed versus the growth time, in accordance with the LSW model as described by eq 3.

limited coarsening. The intercept at $t = 0$ corresponds to the average size of the as-prepared particles.
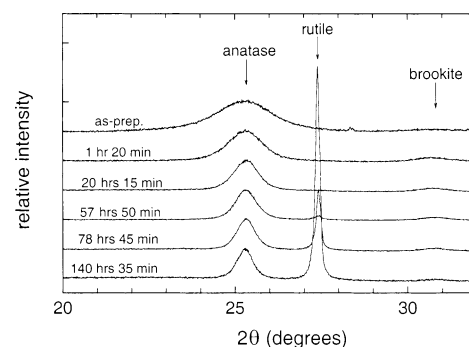

Figure 5. X-ray diffraction patterns for TiO_2 particles as a function of time at 200 °C. The peak positions of anatase, rutile, and brookite are indicated. Note that the diffraction patterns are normalized to the peak height of anatase and that the curves are displaced for clarity.
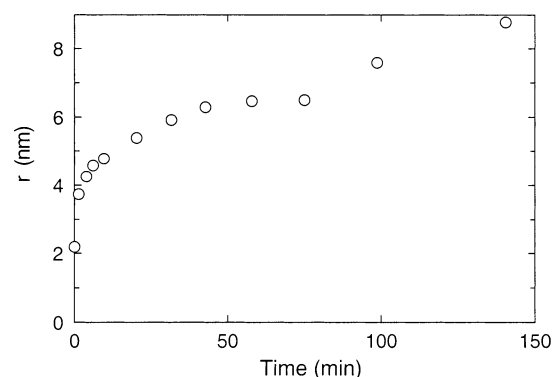

Figure 6. Particle radius versus time obtained from the broadening of the anatase (101) X-ray diffraction peak. The particle size was obtained from $B = k\lambda/(s \cos \theta)$ where B (radians) is the full-width at half-maximum (fwhm) in the 2θ scan, k is a constant (0.94), λ is the X-ray wavelength (1.54 Å for Cu Kα), s is the particle diameter, and θ is the angle of the diffraction peak (degrees). Note that $B = b - \beta$, where b is the experimental fwhm and β is the instrumental broadening (0.06°).

Figure 5 shows X-ray diffraction patterns for TiO_2 particles as a function of the time at 200 °C. It can be seen that the particles consist of anatase and a small fraction of brookite up to a growth time of about 60 h, while at longer times anatase is transformed into rutile. After 140 h, more than 75% of the anatase is transformed to rutile. The width of the anatase (101) peak decreases with time corresponding to an increase in particle size.

The time dependence of the particle size determined from the peak broadening using the Scherrer equation[35] is shown in Figure 6. In all cases the particle size was a factor of 1.5 to 2 larger than obtained from TEM images. Several effects cause the discrepancy. First, the X-ray intensity is proportional to the average particle volume, while the particle size obtained from TEM images represents the average radius.[22] However, the radius obtained from the average particle volume is only about 20% larger than the average radius obtained from the size distributions and only accounts for part of the difference. Second, the size distributions obtained from TEM images were restricted to primary particles and do not include secondary particles formed by epitaxial attachment (see below). Secondary particles are formed from integer multiples of primary particles and can have a significant influence on the volume distribution, even at relatively low concentrations.

Although rutile is the thermodynamically stable bulk phase under ambient conditions, the thermodynamic stability is dependent on particle size, and for particle sizes less than about 14 nm, anatase is more stable than rutile.[36–38] From Figure 5 it
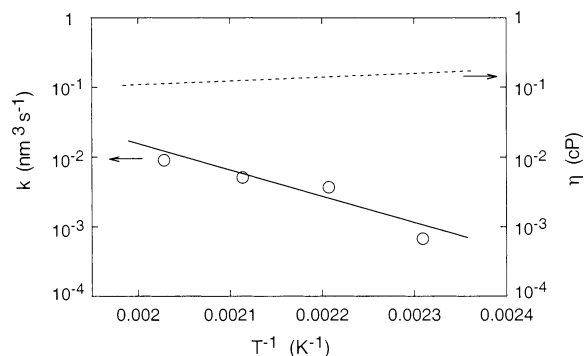
Growth Kinetics of TiO$_2$ Nanoparticles

J. Phys. Chem. B, Vol. 107, No. 8, 2003 **1737**

Figure 7. Arrhenius plot of the rate constant k versus $1/T$ for the growth of anatase particles. The viscosity of water is also shown as a function of temperature.

Figure 8. High-resolution TEM images of anatase particles formed by oriented attachment. Indentations are highlighted by arrows in the upper images. Slight angular misorientations and defects are present in the secondary particle, illustrated by the gray and white lines, which are both drawn parallel to the anatase {101} lattice fringes in the lower image.

can be seen that the rutile peak which emerges after about 60 h, is much narrower than the anatase peak, indicating that the rutile particles are much larger than the anatase particles. This is consistent with a formation mechanism where the anatase-to-rutile transformation is initiated at defects formed at epitaxially attached anatase particles.[23,32,39] In these experiments, anatase is converted to rutile: it should be noted that rutile nanoparticles can also be prepared under the appropriate experimental conditions.[40−42]

The temperature dependence of the coarsening kinetics was determined by preparing particles at temperatures from 160 °C to 220 °C for 16 h. Figure 7 shows the rate constant for coarsening, k, as a function of the inverse temperature. The rate constant increases from about 1×10^{-3} nm^3 s^{-1} at 160 °C to about 1×10^{-2} nm^3 s^{-1} at 200 °C, illustrating that the temperature is an important parameter that can be used to vary the particle size. The activation energy for the coarsening process, obtained from the slope of the Arrhenius plot, is 0.75 eV.

The origin of the temperature dependence of the rate constant can be determined from eq 3 by rewriting the diffusion coefficient in terms of the viscosity according to the Stokes−Einstein equation:

$$D = \frac{RT}{6\pi N_a \eta a} \tag{4}$$

where N_a is Avogadro's constant, η is the viscosity, and a is the hydrodynamic radius of the solvated ion or molecule. Substitution in eq 3 results in the following expression for the rate constant, k:

$$k = \frac{8\gamma V_m^2 c_\infty}{54\pi N_a \eta a} \tag{5}$$

The important system-dependent parameters in eq 5 are γ, V_m, c_∞, and η. The surface energy of rutile is on the order of 1.5 J m^{-2} and is only weakly dependent on temperature.[43] Assuming that the surface energy is proportional to density, then the surface energy of anatase would be expected to be slightly lower. The surface energy at the solid/liquid interface is expected to be on the order of 0.1−1 J m^{-2}, due to adsorbed ions and solvent molecules.[44] The temperature dependence of the molar volume V_m is also expected to be very weak in this temperature range since the thermal expansion coefficient of TiO$_2$ is very small. The temperature dependence of the viscosity η of water is shown in Figure 7.[45] However, the factor 2 change in the viscosity is smaller than the order of magnitude change in the rate constant over the measured temperature range. The final parameter to
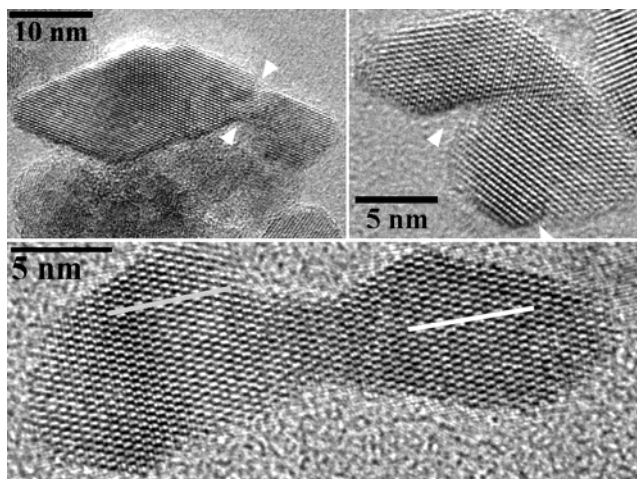
be considered is the equilibrium solubility of TiO$_2$. The equilibrium solubility of TiO$_2$ determined from the rate constants between 160 °C and 220 °C, using $\gamma = 0.1$ J m^{-2}, $V_m = 20.8$ cm^3 mol^{-1}, and $a = 0.5$ nm, is in the range 4×10^{-13} mol L^{-1} to 4×10^{-12} mol L^{-1}. The solubility of TiO$_2$ in phosphate buffer at pH 10 is on the order of 10^{-9} mol L^{-1} at 200 °C and is dependent on phosphate ion concentration.[46] The solubility of TiO$_2$ in acidic solutions is known to be lower, suggesting that the values determined from the rate constants are reasonable. The temperature dependence of the rate constant clearly suggests that the solubility of TiO$_2$ increases with increasing temperature. From these results it can be concluded that the growth kinetics can be further tailored by using a different solvent or complexing agents that could enhance the solubility of TiO$_2$.

In addition to coarsening, the particle size distribution in the system can also be modified by epitaxial attachment of one or more primary particles leading to the formation of secondary particles. The driving force for the assembly process is the reduction of surface energy, and this mechanism has been reported previously for a variety of metal oxide systems.[28,32,33] Figure 8 shows high-resolution TEM images of secondary particles. These particles have irregular shapes with regions of positive and negative curvature characteristic of epitaxial attachment. In the upper two images, indentations in the particle morphology (indicated by the arrows) and slight angular misorientations are present in the secondary particle.

The lattice fringes observed in the images can be directly related to the crystal structure of the particles. The gray line in Figure 8, which is drawn parallel to the anatase {101} lattice fringes on the left-hand side of the particle, is slightly inclined to the white line, which is also parallel to the {101} fringes on the right-hand side. This slight misorientation suggests that defects are introduced into the particle during the assembly process since the primary particles are defect-free.

The attachment mechanism can be evaluated by determining the number of secondary particles and the number of primary particles per secondary particle with time and temperature. Figure 9a shows the average attachment order, which is defined as the average number of primary particles per secondary particle, as a function of growth time at 160 °C and 200 °C. It can be seen that the average attachment order increases with time, indicating that secondary particles continue to grow by
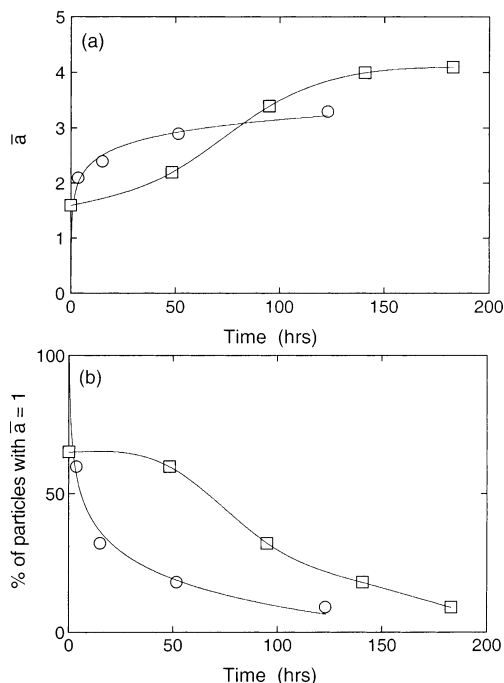
Figure 9. The average assembly order, $\bar{a}$, and the percentage of particles with an assembly order of 1 as a function of aging time and temperature. The average assembly order is defined as the number of primary particles per secondary particle, and was determined by analyzing a minimum of 100 secondary particles. Note that only particles showing a clearly observable assembly process were included in the count.

oriented attachment during the coarsening process. These results lend additional support to the hypothesis that particles grow by coarsening and assembly, as opposed to coarsening alone. Figure 9b shows the percentage of particles with an attachment order of 1 versus time. The results show the same trend for the attachment process, and indicate that the process is faster at higher temperature. However, attachment can occur even at relatively low temperatures, which is illustrated by the average attachment order of 1.6 for the as-prepared sample.

Attachment processes may have a pronounced effect on the growth kinetics of nanoparticles. For example, secondary particles are much larger than primary particles, thus changing the particle size distribution. The particle size distribution provides the basis for further growth of the large particles. It should be noted that the particle sizes reported in Figures 2 and 3 determined with TEM represent the size of primary particles, i.e., secondary particles were not included. However, in the X-ray measurements the secondary particles may have had a significant influence on the average particle size determined from the peak width.

In summary, the average size of primary particles in this system is dependent on coarsening. Parameters that influence coarsening include time, temperature, and solution chemistry. For example, the growth kinetics of both primary and secondary particles can be further modified using different anions, solvents, pH, or concentration, since these parameters may affect the equilibrium solubility, the viscosity, the particle shape, as well as the energy gain for oriented attachment.

References and Notes

(1) Manna, L.; Scher, E. C.; Alivisatos, A. P. *J. Am. Chem. Soc.* **2000**, *122*, 12700.

(2) Guzelian, A. A.; Banin, U.; Lee, J. C.; Alivisatos, A. P. In *Advances in Metal and Semiconductor Clusters*; Duncan, M. A., Ed.; 1998; Vol. 4, p 1.

(3) Empedocles, S. A.; Neuhauser, R.; Shimizu, K.; Bawendi, M. G. *Adv. Mater.* **1999**, *11*, 1243.

(4) Murray, C. B.; Kagan, C. R.; Bawendi, M. G. *Annu. Rev. Mater. Sci.* **2000**, *30*, 545.

(5) Nirmal, M.; Brus, L. *Acc. Chem. Res.* **1998**, *32*, 407.

(6) Yang, P.; Zhao, D.; Margolese, D. I.; Chmelka, B. F.; Stucky, G. D. *Nature* **1998**, *396*, 152.

(7) Zaban, A.; Aruna, S. T.; Tirosh, B. A.; Gregg, B. A.; Mastai, Y. *J. Phys. Chem. B* **2000**, *104*, 4130.

(8) Zhang, Z.; Wang, C.-C.; Zakaria, R.; Ying, J. Y. *J. Phys. Chem. B* **1998**, *102*, 10871.

(9) Matijevic, E. *Annu. Rev. Mater. Sci.* **1985**, *15*, 483.

(10) Henglein, A. *Top. Curr. Chem.* **1988**, *143*, 113.

(11) Matijevic, E. *Langmuir* **1986**, *2*, 12.

(12) Livage, J.; Henry, M.; Sanchez, C. *Prog. Solid State Chem.* **1988**, *18*, 259.

(13) Sugimoto, T. *Adv. Colloid Interface Sci.* **1987**, *28*, 65.

(14) Anderson, M. A.; Gieselmann, M. J.; Xu, Q. *J. Membr. Sci.* **1988**, *39*, 243.

(15) O'Regan, B.; Grätzel, M. *Nature* **1991**, *353*, 737.

(16) Kormann, C.; Bahnemann, D. W.; Hoffmann, M. R. *J. Phys. Chem.* **1988**, *92*, 5196.

(17) (a) Barringer, E. A.; Bowen, H. K. *Langmuir* **1985**, *1*, 414. (b) Barringer, E. A.; Bowen, H. K. *Langmuir* **1985**, *1*, 420.

(18) Jean, J. H.; Ring, T. A. *Langmuir* **1986**, *2*, 251.

(19) (a) Look, J.-L.; Zukoski, C. F. *J. Am. Ceram. Soc.* **1992**, *75*, 1587. (b) Look, J.-L.; Zukoski, C. F. *J. Am. Ceram. Soc.* **1995**, *78*, 21.

(20) Vorkapic, D.; Matsoukas, T. *J. Am. Ceram. Soc.* **1998**, *81*, 2815.

(21) Vorkapic, D.; Matsoukas, T. *J. Colloid Interface Sci.* **1999**, *214*, 283−291.

(22) Penn, R. L.; Banfield, J. F. *Geochim. Cosmochim. Acta* **1999**, *63*, 1549.

(23) Barbé, C. J.; Arendse, F.; Comte, P.; Jirousek, M.; Lenzmann, F.; Shklover, V.; Grätzel, M. *J. Am. Ceram. Soc.* **1997**, *80*, 3157.

(24) Matijevic, E. *J. Phys. Chem. B* **2001,** *105,* 11630.

(25) Bahnemann, D. W.; Kormann, C.; Hoffmann, M. R. *J. Phys. Chem.* **1987**, *91*, 3789.

(26) Wong, E. M.; Bonevich, J. E.; Searson, P. C. *J. Phys. Chem. B* **1998**, *102*, 7770.

(27) Schwertmann, U.; Cornell, R. M. *Iron Oxides in the Laboratory: Preparation and Characterization*; Weinheim: New York, 1991.

(28) Penn, R. L.; Oskam, G.; Strathmann, T. J.; Searson, P. C.; Stone, A. T.; Veblen, D. R. *J. Phys. Chem.* **2001**, *105*, 2177.

(29) Greenwood, G. W. *Acta Metall.* **1956**, *4*, 243.

(30) Lifshitz, I. M.; Slyozov, V. V. *J. Phys. Chem. Solids* **1961**, *19*, 35.

(31) Wagner, C. *Z. Elektrochem.* **1961**, *65*, 581.

(32) Penn, R. L.; Banfield, J. F. *Science* **1998**, *281*, 969.

(33) Alivisatos, A. P. *Science* **2000**, *289*, 736.

(34) Reimer, L. *Energy-Filtering Transmission Electron Microscopy*; Springer-Verlag: Berlin, 1995.

(35) Jenkins, R.; Snyder, R. L. *Introduction to X-ray Powder Diffractometry*, Chemical Analysis; Winefordner, J. D., Ed.; Wiley: New York, 1996; Vol. 138.

(36) Zhang, H.; Banfield, J. F. *J. Mater. Chem.* **1998**, *8*, 2073.

(37) Zhang, H.; Banfield, J. F. *J. Phys. Chem.* **2000**, *104*, 3481.

(38) Gribb, A. A.; Banfield, J. F. *Am. Mineral.* **1997**, *82*, 717.

(39) Penn, R. L.; Banfield, J. F. *Am. Mineral.* **1999**, *84*, 871.

(40) Matijevic, E.; Budnik, M.; Meites, L. *J. Colloid Interface Sci.* **1977**, *61*, 302.

(41) Wang, C.-C.; Ying, J. Y. *Chem. Mater.* **1999**, *11*, 3113.

(42) Park, N.-G.; van de Lagemaat, J.; Frank, A. J. *J. Phys. Chem. B* **2000**, *104*, 8989.

(43) Terwilliger C. D.; Chiang, Y. *J. Am. Ceram. Soc.* **1995**, *78*, 2045.

(44) Zangwill, A. *Physics at Surfaces*; Cambridge University Press: Cambridge, 1988,

(45) *NBS/NRC Steam Tables*; Haar, L., Gallagher, J. S., Kell, G. S., Eds.; NSRDS: 1984; p 263.

(46) Ziemniak, S. E.; Jones, M. E.; Combs, K. E. *J. Solution Chem.* **1993**, *22*, 601.